# Nanoscale Mapping of Lithium-Ion Diffusion in a Cathode within an All-Solid-State Lithium-Ion Battery by Advanced Scanning Probe Microscopy Techniques

Jing Zhu, Li Lu, and Kaiyang Zeng*

Department of Mechanical Engineering, National University of Singapore, 9 Engineering Drive 1, Singapore 117576

ABSTRACT High-resolution real-space mapping of Li-ion diffusion in the $LiNi_{1/3}Co_{1/3}Mn_{1/3}O_2$ cathode within an all-solid-state thin film Li-ion battery has been conducted using advanced scanning probe microscopy techniques, namely, band excitation electrochemical strain microscopy (BE-ESM) and conductive atomic force microscopy. In addition, local variations of the electrochemical response in the $LiNi_{1/3}Co_{1/3}Mn_{1/3}O_2$ thin film cathode at different cycling stages have been investigated. This work demonstrates the unique feature and applications of the BE-ESM technique on battery research. The results allow us to establish a direct relationship of the changes in ionic mobility as well as the electrochemical activity at the nanoscale with the numbers of charge/discharge cycles. Furthermore, various factors influencing the BE-ESM measurements, including sample mechanical properties (*e.g.*, elastic and dissipative properties) as well as surface electrical properties, have also been studied to investigate the coupling effects on the electrochemical strain. The study on the relationships between the Li-ion redistribution and microstructure of the electrode materials within thin film Li-ion battery will provide further understanding of the electrochemical degradation mechanisms of Li-ion rechargeable batteries at the nanoscale.
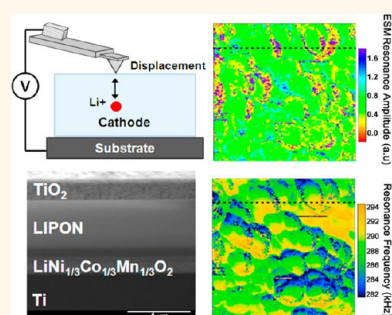
KEYWORDS: electrochemical strain microscopy · conductive AFM · thin film Li-ion battery · $LiNi_{1/3}Co_{1/3}Mn_{1/3}O_2$

Rechargeable Li-ion batteries are the most practical and widely used power sources for portable and mobile applications due to their evident advantages, such as high energy density, long cycle life, little memory effect, and good design flexibility.[1-3] As the demand for more powerful and durable electronic devices in today's information-rich society increases, the optimization of both energy density and cyclability of Li-ion batteries requires comprehensive understanding of the electrochemical mechanisms from nano-, micro-, to macroscales. Since classical electrochemical techniques, such as potentiostat and electrochemical impedance spectroscopy, are vitally limited at the nanoscale, various scanning probe microscopy (SPM) techniques have been developed and applied to investigate the nanoscale electrochemical functionalities and aging mechanisms of Li-ion batteries in recent years.[4,5] It is now believed that the aging phenomena of Li-ion batteries are attributed to the strain induced by the volumetric changes and lattice distortion upon Li-ion intercalation/deintercalation during electrochemical reactions.[6] Recently, a new SPM technique, namely, electrochemical strain microscopy (ESM), was developed and applied to Li-ion batteries to investigate the broad spectrum of the local electrochemical phenomena in battery systems. These phenomena include electrochemical strain (defined as surface displacement due to the electrochemical process), ionic mobility, distribution of Li-ion diffusion path, electrochemical activity, effects of structural and surface defects, and many others.[7-14]

The operation principle of the ESM technique is very similar to the well-known piezoresponse force microscopy (PFM) with the major difference of the bias strain (deformation) coupling mechanism. The PFM technique measures the electromechanical
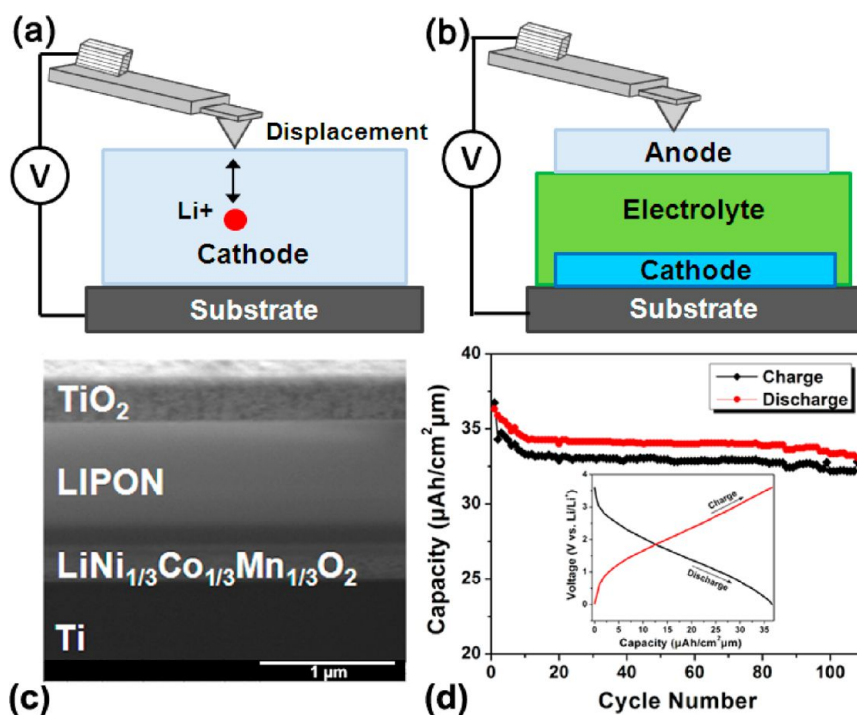
Figure 1. (a) Schematic of ESM operation principle on a single battery element (Li-ion-contained cathode). (b) Schematic of ESM measurement on a full battery structure. (c) FIB cross-sectional image, and (d) charge/discharge cycling performance of the all-solid-state thin film Li-ion battery.

strain induced by piezoelectric response due to an applied electrical bias, while ESM detects the local electrochemical strain originated from bias-induced ionic diffusion and the related molar volume change in the battery materials.[15−18] Figure 1a,b shows the operation principle of the ESM technique on a single electrode (Li-contained cathode) or a full battery structure (top anode), respectively. In the ESM approach, bias is applied through the conductive tip to induce a concentrated electrical field in a nanoscale volume of material near the tip−sample contact, leading to the changes of electrochemical potential of a lithium ion and thus the ionic diffusion and redistribution inside this small volume of material. The changes in the ionic concentration can result in the molar volume change and oscillatory surface displacement of battery material. Using a lock-in technique, the amplitude of oscillatory displacement is detected as the electrochemical strain, which is directly related to the Li-ion diffusion. In order to further amplify the weak dynamic displacement (∼pm), ESM mapping is usually performed with the band excitation (BE) mode for signal enhancement on the resonance frequency of the cantilever. Note that at high measurement frequencies in the BE mode (∼290 kHz compared to ∼1 Hz Li-ion diffusion frequency), the enhanced BE-ESM response is a direct result of the Li-ion concentration change in the probed volume, which is induced by both ionic diffusion (concentration-driven) and ionic migration (field-driven) during Li-ion intercalation/deintercalation process.[8,14] In the BE approach, the tip is excited using a signal spanning a frequency band,

and the responses at this frequency band are simultaneously monitored.[16] The resulting amplitude *versus* frequency and phase *versus* frequency curves are collected at each point (128 × 128 point array in this work) and stored in 3-D data arrays (*x.y.* and amplitude and *x,y* and phase). All response curves are fitted using the damped simple harmonic oscillator (SHO) model, which is described by three independent parameters, namely, resonant frequency (ω_0), amplitude at the resonance (A_{max}), and quality factor (Q), that describe the energy loss in the system. Their relationship can be described by the following equation:[19,20]

$$A(\omega) = \frac{A_{max}\omega_0^2/Q}{\sqrt{(\omega_0^2 - \omega^2)^2 + (\omega_0\omega/Q)^2}}$$

where ω_0 and A are closely related to the tip−sample force gradient and the driving force, respectively. Most importantly, the application of the BE-ESM technique requires the calibration of the frequency response of the cantilever. Without the calibration of the cantilever, the ESM images may not demonstrate normal cantilever-dependent contrast, especially the quality factor. Note that the energy dissipation due to tip−sample interactions is determined by $P_{diss} = P_{drive} - P_0$, where P_{drive} is the energy provided to the cantilever by an external driving force, and P_0 is the intrinsic energy loss within the cantilever material due to the cantilever damping, which can be determined by the calibration at reference position as $P_{diss} = 0$.[21]
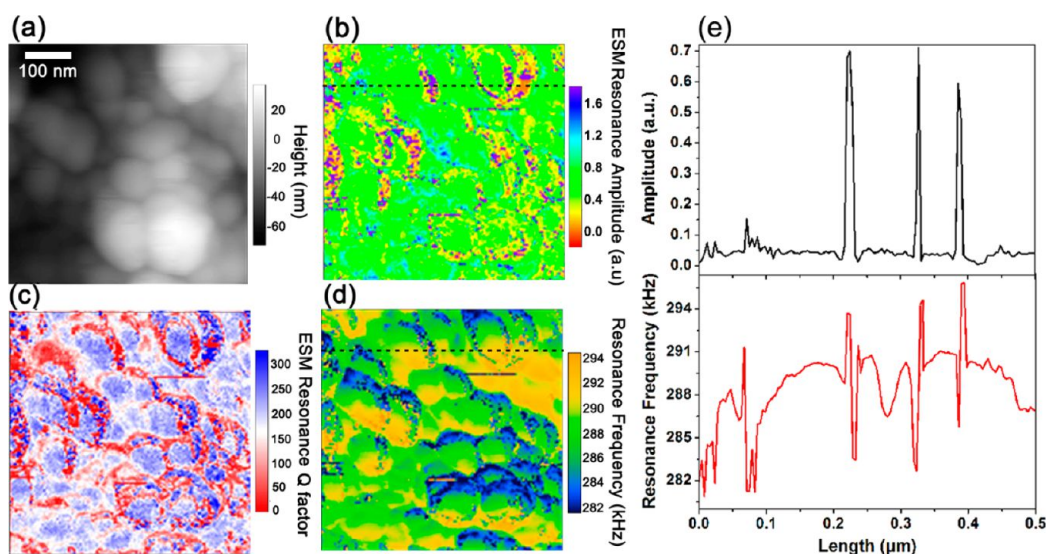
Figure 2. (a) Surface topography; BE-ESM maps of (b) resonance amplitude; (c) resonance quality factor (Q-factor); (d) contact resonance frequency; and (e) line section profiles in amplitude and resonance frequency, corresponding to the lines in (b) and (d) of the $LiNi_{1/3}Co_{1/3}Mn_{1/3}O_2$ thin film cathode.

In this study, a novel all-solid-state thin film Li-ion microbattery, consisting of TiO_2 anode, LiPON electrolyte, and $LiNi_{1/3}Co_{1/3}Mn_{1/3}O_2$ cathode, is selected as the test system. The structure of the microbattery is verified by cross-sectional image obtained by focused ion beam (FIB) cutting (Figure 1c). In this novel thin film microbattery, layered $LiNi_{1/3}Co_{1/3}Mn_{1/3}O_2$ with specific composition is a promising cathode material due to its larger capacity, higher safety, and lower toxicity compared to those of a traditional $LiCoO_2$ cathode.[22−32] On the other hand, a nanocrystalline TiO_2 anode, a representative intercalation/deintercalation-based anode, shows very different electrochemical response/strain from those in the traditional anode materials, such as carbon, silicon, and alloys.[33−37] As shown in Figure 1d, the fabricated thin film microbattery has fully electrochemical functionality (reversible charge/discharge capability and good cycling performance) once the Au current collector is deposited on top of the anode. The charge/discharge curve exhibits a characteristic shape which depends on the electrochemical potential plateaus of the TiO_2 anode (∼1.75 V vs Li/Li-ion) and $LiNi_{1/3}Co_{1/3}Mn_{1/3}O_2$ cathode (∼3.70 V vs Li/Li-ion) (inset in Figure 1d).

In this work, nanoscale mapping of the ionic diffusion has been conducted on the $LiNi_{1/3}Co_{1/3}Mn_{1/3}O_2$ thin film cathode (single battery element). This mapping allows us to establish the direct relationships between the electrochemical strain and structural heterogeneities for cathode thin films. Furthermore, since the capacity fading of the electrode material can be attributed to the development of electrochemical strain as well as the variations of ionic diffusion dynamics, BE-ESM measurements were also conducted on $LiNi_{1/3}Co_{1/3}Mn_{1/3}O_2$ thin film cathodes after different charge/discharge cycles, so that the effects of

galvanostatic cycling on electrochemical strain and activity were also investigated. It should be noted that the evolution of electrochemical strain during cycling is influenced by several factors, including ionic diffusion coefficient, mechanical properties (elastic and dissipative), and electrical properties (surface conductivity) of the sample surface; thus, conductive AFM (c-AFM) was also used in this study, and the results are discussed together with that from the BE-ESM measurements.

RESULTS AND DISCUSSION

First, BE-ESM mapping was conducted on as-deposited the $LiNi_{1/3}Co_{1/3}Mn_{1/3}O_2$ thin film cathode. The structure of this cathode material has been confirmed to be a hexagonal α-$NaFeO_2$ type structure with the preferred crystallographic orientation of (003) and (104) by using X-ray diffraction (XRD). Thus, the lithium ion can be easily transported under an electrical field through the oriented ionic diffusion planes in the structure. Figure 2a shows a high-resolution topographical image of the polycrystalline $LiNi_{1/3}Co_{1/3}Mn_{1/3}O_2$ thin film cathode, which consists of columnar grains with the average grain size of ∼100 nm. The surface roughness (rms) is around ∼12 nm, due to the presence of deep cavities and grain boundaries. Panels b−d of Figure 2 show the BE-ESM mapping of the resonance amplitude, resonance quality factor (Q-factor), and resonance frequency, respectively. Features less than 10 nm can be clearly observed from the images, providing the high-resolution imaging capability of the BE-ESM technique. Figure.2b shows that the amplitude on resonance frequency is not homogeneous across the sample surface and changes abruptly at boundary-like features, indicating clear variations of ionic mobility and electrochemical activity

across grain boundaries (also shown in Figure 2e). Additionally, it is found that some "nanospots" concentrate at certain grain boundaries and show strong amplitude signal (deep purple color), indicating enhanced Li-ion diffusion and accumulation in these regions. It is noted that the amplitude of oscillatory surface displacement, which is defined as the electrochemical strain, is directly related to the changes of Li-ion concentration induced by the high-frequency tip bias. Therefore, the electrochemical strain mapping can provide important information on the variations of bias-induced Li-ion diffusion and redistribution, also establishing the direct relationship between the preferred Li-ion diffusion paths and microstructure of the $LiNi_{1/3}Co_{1/3}Mn_{1/3}O_2$ thin film cathode at the nanoscale; that is, lithium ions are more concentrated at grain boundary regions. Besides the detection of electrochemical strain, a significant feature of BE-ESM is the capability to map the surface mechanical properties at the nanoscale, which is similar to that obtained from atomic force acoustic microscopy.[16] More specifically, Q-factor (peak width in the BE-ESM signal) is a measurement of the dissipative energy due to the tip−sample interactions, providing fundamental information on mechanical dissipative properties,[15] while the resonance frequency is a measurement of the conservative tip−sample interactions, providing information on local elastic properties of the sample surface. As shown in Figure 2c, the resonance Q-factor mapping shows very strong variations (∼300) between the grains and the grain boundaries, corresponding well to the surface topography differences. It is observed that Q-factor decreases at grain boundaries (red color) and increases at areas within the individual grains (blue color); this indicates higher energy dissipation at the topographical depressions and lower energy dissipation at the protrusions. Similarly, the resonance frequency mapping (Figure.2d) also largely corresponds to the surface topographical features. It is observed that the resonance frequency increases at topographical depressions (yellow color) and decreases within grains but at the area adjacent to the grain boundaries (blue color). The variation of resonance frequency due to the grain structure and surface roughness is on the order of ∼15 kHz compared with ∼290 kHz drive frequency (this will be discussed further together with the results from cycled samples in the later sections). Therefore, the topographical depressions (e.g., grain boundaries) can increase the effective tip−sample contact area, resulting in higher contact stiffness (large resonance frequency) and larger energy dissipation (small Q-factor). In addition, Figure 2e shows line section profiles in both amplitude and resonance frequency images. It is obvious that the contact resonance frequency slightly changes within individual grains but increases abruptly across the grain boundary regions, corresponding to high

amplitude of surface displacement, hence the high Li-ion concentration and enhanced ionic diffusion at these regions.

It is known that the electrochemical activity of electrode material gradually changes during charge/discharge cycling, resulting in the capacity fading and electrochemical degradation. Therefore, in this study, in order to investigate the effects of galvanostatic cycling on the variations of electrochemical strain as well as the Li-ion diffusion dynamics, BE-ESM is further conducted on cycled the $LiNi_{1/3}Co_{1/3}Mn_{1/3}O_2$ thin film cathode at different cycling stages. First of all, the electrochemical mechanisms of $LiNi_{1/3}Co_{1/3}Mn_{1/3}O_2$ upon Li-ion intercalation/deintercalation should be stated clearly. Note that, in hexagonal structure $LiNi_{1/3}Co_{1/3}Mn_{1/3}O_2$, the transition metal sites (3a) are equally occupied by nickel, manganese, and cobalt atoms, the alkali sites (3b) are occupied by lithium atoms, and the 6c sites are occupied by oxygen atoms. The valences of nickel, cobalt, and manganese ions are 2+, 3+, and 4+, respectively. Among them, only divalent nickel ions (Ni^{2+}) and trivalent cobalt ions (Co^{3+}) are electroactive. According to previous X-ray absorption spectroscopy (XAS) analysis,[38] an intermediate state of Ni^{3+} can be observed during charge/discharge cycling. Thus, the electrochemical mechanism of $LiNi_{1/3}Co_{1/3}Mn_{1/3}O_2$ is a two-step redox reaction involving Ni^{2+}/Ni^{3+} and Ni^{3+}/Ni^{4+} upon Li-ion intercalation/deintercalation. In addition, through ex situ XRD studies,[31] there is no obvious structure change (new phase appearance) observed after 100 cycles, indicating good structural stability during cycling. In summary, after charge/discharge cycles, there is no significant change in chemical composition and microstructure in the $LiNi_{1/3}Co_{1/3}Mn_{1/3}O_2$ cathode. Panels a-c of Figure 3 show the BE-ESM mapping of $LiNi_{1/3}Co_{1/3}Mn_{1/3}O_2$ thin film cathodes after 10, 50, and 100 charge/discharge cycles, respectively. In Figure 3, the columns from left to right are resonance amplitude images, resonance Q-factor images, and line section profiles from the selected lines in the amplitude image. Compared with the BE-ESM mapping on the as-deposited $LiNi_{1/3}Co_{1/3}Mn_{1/3}O_2$ thin film cathode, the variations of electrochemical strain during charge/discharge cycling are clearly observed. First, grain-boundary-related nanospots in Figure 2b, which is associated with highly localized Li-ion diffusion and redistribution, have disappeared after the cycling process. After 100 cycles, besides some deep cavities, even the BE-ESM enhanced signal at the grain boundaries cannot be clearly observed. Second, the as-deposited sample has evidently higher BE-ESM response (in absolute value) compared to that of the cycled samples, as shown in the amplitude scale bar. Third, through the comparison of amplitude line section profiles, the variations of amplitude between topographical depressions and protrusions have become smaller with increasing of the cycling number, corresponding to the lower contrast
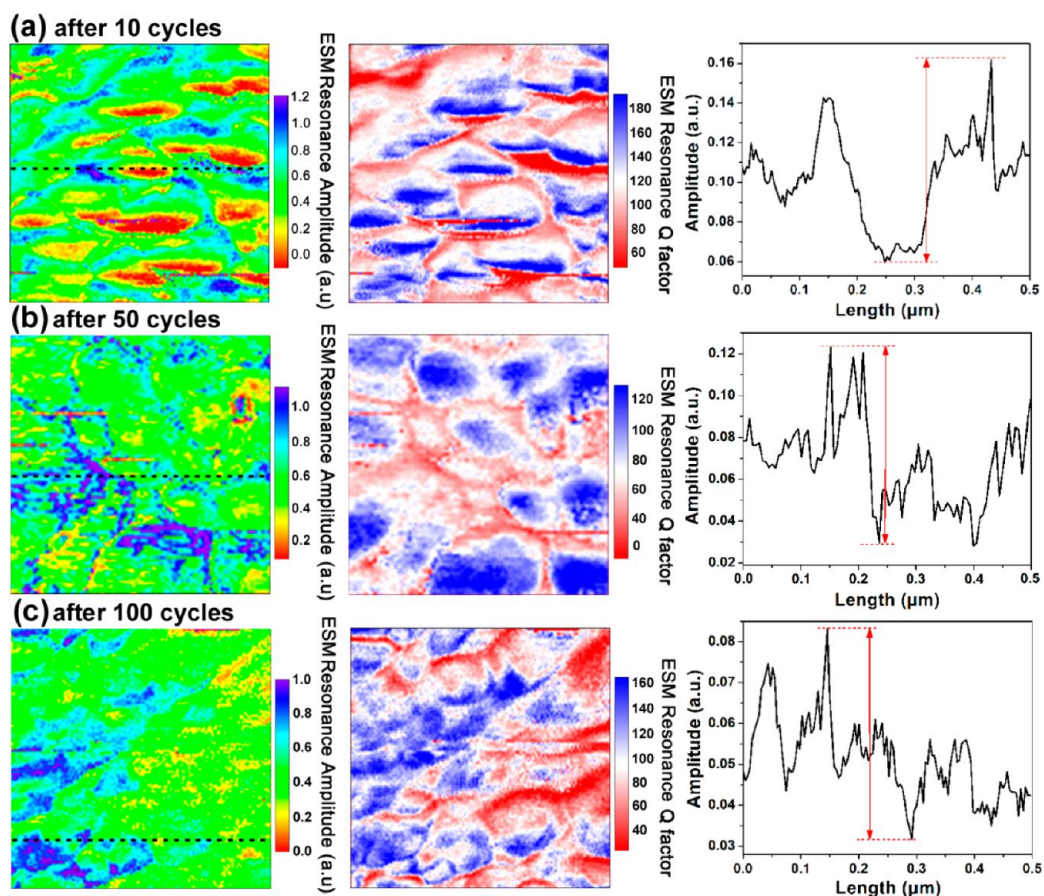
Figure 3. BE-ESM maps of resonance amplitude and Q-factor of the LiNi$_{1/3}$Co$_{1/3}$Mn$_{1/3}$O$_2$ thin film cathode at different cycling stages: (a) 10 cycled, (b) 50 cycled, and (c) 100 cycled, as well as the line section profiles of resonance amplitude. The left column is the amplitude map; the middle column is the Q-factor map, and the right column is the line section profile of the amplitude maps, corresponding to the lines in the left column.

in the amplitude images. All of these gradual changes are shown to be functions of cycling number, and it can be explained by the degradation in electrochemical activity upon Li-ion intercalation/deintercalation processes in the LiNi$_{1/3}$Co$_{1/3}$Mn$_{1/3}$O$_2$ thin film cathode, especially at boundary regions. Through the comparison of the as-deposited and aged LiNi$_{1/3}$Co$_{1/3}$Mn$_{1/3}$O$_2$ thin film cathodes (after 100 cycles), it is obvious that the decrease of Li-ion concentration is localized at the grain boundary regions, which illustrates the weak enhancement of the Li-ion diffusion and accumulation at these regions after cycling, corresponding to reduced electrochemical activity after cycling process. In addition, the decrease of contrast at grain boundaries in BE-ESM amplitude is more evident after the first 10 cycles (Figure 2e), which can be understood from more significant electrochemical degradation during the initial charge/discharge cycles. Furthermore, combining resonance amplitude and Q-factor images, the correlation between electrochemical strain and energy dissipation can be locally established. According to Chen *et al.*, Q-factor is closely related to the total energy dispassion induced by Li-ion redistribution and thus can reflect the energy barriers for Li-ion intercalation/deintercalation

within the battery materials.[39] As shown in Figure 2 and Figure 3, the scanned region in the as-deposited LiNi$_{1/3}$Co$_{1/3}$Mn$_{1/3}$O$_2$ thin film cathode has higher Q-factor and also relatively larger amplitude on average (indicated in the scale bar). It can be understood that higher Q-factor corresponds to smaller energy dissipation, indicating smaller energy barriers for Li-ion intercalation/deintercalation for the as-deposited sample. Since the energy barriers increase with the increase of cycling number, Li-ion intercalation/deintercalation has become more difficult, resulting in lower Li-ion diffusivity and electrochemical activity, thus smaller electrochemical strain.

In general, the variations of BE-ESM amplitude during the charge/discharge cycling process can be explained by several factors, such as (i) differences in Li-ion diffusion coefficient; (ii) differences in sample mechanical properties; and (iii) differences in sample electrical properties, such as surface conductivity. First, as discussed earlier, the variations of BE-ESM amplitude are directly related to the changes in Li-ion concentration, which is mainly determined by Li-ion diffusion coefficient and electrochemical activity at different cycling stages. Second, considering Hooke's law, if the
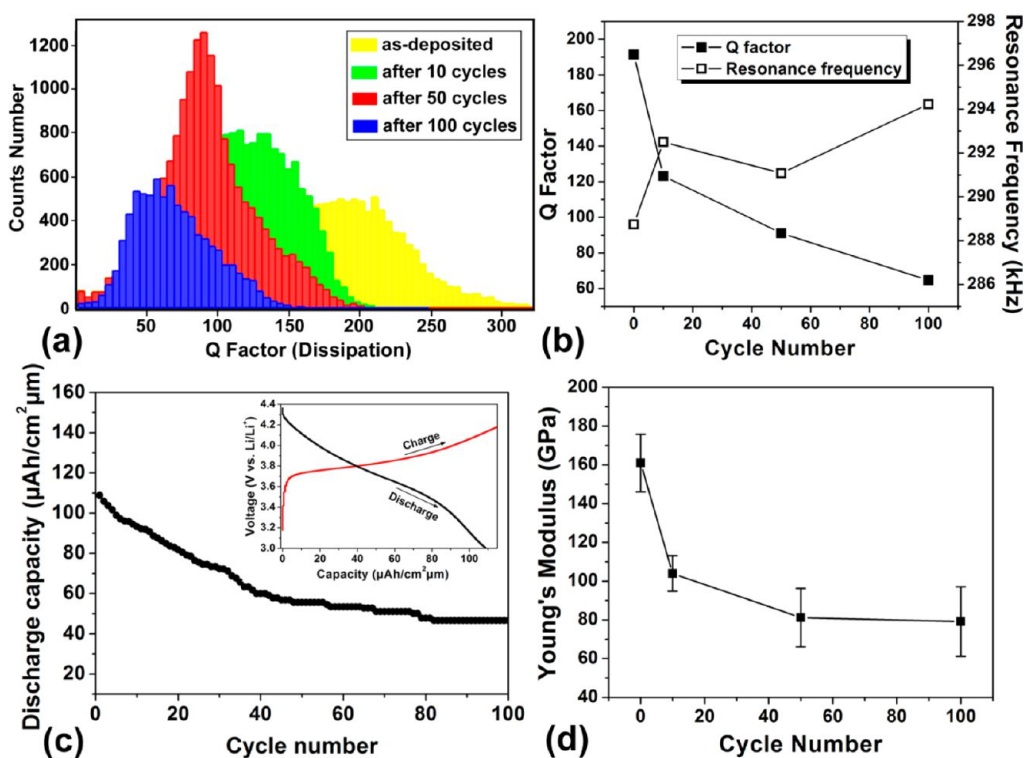
Figure 4. (a) Histograms of resonance Q-factor distribution of the $LiNi_{1/3}Co_{1/3}Mn_{1/3}O_2$ thin film cathode at different cycling stages; (b) changes of resonance frequency and Q-factor *vs* cycling number; (c) charge/discharge cycling performance of the $LiNi_{1/3}Co_{1/3}Mn_{1/3}O_2$ thin film cathode; the inset is the voltage−capacity profile during the first charge/discharge cycle; and (d) nanoindentation measured Young's modulus *vs* cycling number.

volume changes induced by Li-ion diffusion are constant, the measured amplitude of the surface displacement is effectively influenced by sample mechanical properties; for example, a harder sample surface with higher contact stiffness shows smaller surface displacement (induced by volume change) compared to that from the softer surface. Therefore, the differences in the surface mechanical properties are expected to have significant effects on the measured electrochemical strain (BE-ESM amplitude). This is confirmed by the results from this study; that is, there is a strong coupling between the surface topography and mechanical properties of the sample surface (Figures 2 and 3), such as dissipative (Q-factor) and conservative properties (resonance frequency). Figure 4a shows the histograms of Q-factor distribution of the $LiNi_{1/3}Co_{1/3}Mn_{1/3}O_2$ thin film cathode at different cycling stages. In the BE-ESM analysis, Q-factor is a dimensionless parameter, which characterizes the peak width of the resonance frequency of the cantilever (to its center frequency). Since Q-factor is defined as the ratio of the energy stored in the system to the energy generated, lower Q-factor indicates larger energy loss relative to energy storage, corresponding to higher damping. In addition, it is well-known that the contact resonance frequencies can be converted into the contact stiffness by considering the dynamics of a clamped-spring coupled cantilever and then further converted into local storage modulus

by considering effective tip−sample contact geometry and indentation modulus.[40,41] In the BE-ESM method, relative contact stiffness can be directly extracted by measuring the resonance frequency shift from the free-resonance frequency of the cantilever vibrated in air.[42] Figure 4b shows the relative changes of the BE-ESM resonance frequency and Q-factor as functions of galvanostatic cycling number for the $LiNi_{1/3}Co_{1/3}Mn_{1/3}O_2$ thin film cathode. All of these values are obtained by SHO fitting and averaged across a scanned area of 500×500 nm^2. Figure 4c shows the corresponding charge/discharge cycling performance of the $LiNi_{1/3}Co_{1/3}Mn_{1/3}O_2$ thin film cathode between 3.0 and 4.3 V at a constant current density for comparison. As a result, the resonance frequency slightly decreases only by ∼6 kHz after 100 cycles, which is even smaller than the resonance peak width (∼10 kHz) and the variations of the resonance frequency across the scanned area (∼15 kHz), which is due to the presence of grain structure and surface roughness (Figure 2d). Therefore, it is reasonable to believe that the resonance frequency remains approximately constant, indicating almost unchanged effective stiffness through the tip−sample junction during the cycling. In this case, since the effects of contact stiffness on the measured ESM amplitude are small, the changes in Li-ion concentration should play more significant roles. In addition, the averaged Q-factor significantly decreases from ∼190 to ∼60 after 100 cycles, indicating larger
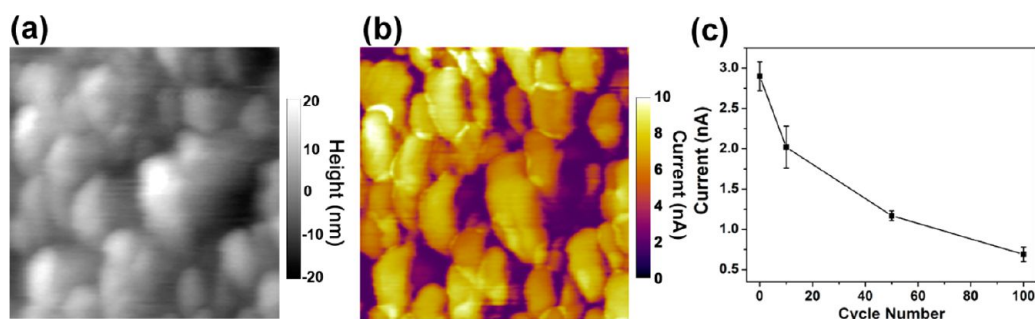
Figure 5. (a) Surface topography; (b) corresponding conductance maps on the as-deposited LiNi$_{1/3}$Co$_{1/3}$Mn$_{1/3}$O$_2$ thin film cathode from the c-AFM measurements; and (c) average values of current *vs* cycling number.

energy dissipation with the increase of cycling number (Figure 4b). It is also noted that the decrease of Q-factor is more significant during the initial cycles; the average decrease rate is ~3.56% per cycle in the first 10 cycles and only ~0.53% per cycle from 10 to 100 cycles. It is interesting to notice that the capacity fading rate is ~1.44% in the first 10 cycles and only ~0.55% per cycle from 10 to 100 cycles (Figure 4c), suggesting that there may be a certain relationship between the capacity fading and the changes in sample dissipative properties (Q-factor). In BE-ESM measurement, the weak surface displacement can be amplified using the cantilever resonance.[42] The amplitude of oscillatory surface displacement A can be amplified to A^* on the cantilever resonance frequency, according to the relationship of $A^* = QA$. Therefore, two factors contribute to the measured ESM amplitude on resonance, that is, the real surface displacement A and the cantilever damping property Q. Since the measured A^* can originate from a change in A (sample property) or a change in Q (cantilever property), both decreases in ionic concentration and the Q-factor are effectively lowering the measured resonance amplitude; however, it is still difficult to distinguish these two contributions unambiguously. In summary, with the increase of cycling number, the LiNi$_{1/3}$Co$_{1/3}$Mn$_{1/3}$O$_2$ thin film cathode exhibits similar conservative elastic properties but very different energy dissipative properties.

It is also well-known that the local surface mechanical properties can vary considerably from the bulk mechanical properties of the samples. As shown in Figure 4d, the nanoindentation measurements show that the Young's modulus of the LiNi$_{1/3}$Co$_{1/3}$Mn$_{1/3}$O$_2$ thin film cathode decreases with the increase of cycling number, evidently in the first 10 cycles; however, there is no significant change in the contact resonance frequency from the BE-ESM measurement (Figure 4b). Note that the contact resonance frequency can qualify the material's ability to store the energy elastically, that is, storage modulus (E'), while Q-factor can qualify the material's ability to damp out energy, that is, loss modulus (E''). During the nanoindentation experiment, the Young' modulus (E^*) measured through the indenter oscillating is a complex dynamic modulus, which is a phase vector incorporating both capabilities (i.e., $E^* = E' + iE''$),

where i is the imaginary unit.[40] Therefore, for materials with significant damping behavior, the Young's modulus (E^*) is not equivalent to the storage modulus (E'). The BE-ESM results suggest that the dissipation loss plays a more significant role in the changes of Young's modulus of the thin film electrode during the charge/discharge cycling. Additionally, since BE-ESM applies very low force (~nN compared to ~mN in nanoindentation) in a very small volume, resulting in a stress field just below the film surface (~nm), the measured local surface elasticity is also sensitive to the crystallographic orientation, surface features, and tip–sample contact characteristics.

As mentioned earlier, the changes in Li-ion concentration during BE-ESM measurement includes both ionic diffusion (concentration-driven) and ionic migration (field-driven) at high frequencies. Among these, the effect of electrical-field-driven migration largely depends on the sample electrical properties and tip–sample contact characteristics. It is known that the tip–sample contact characteristic (e.g., contact resistance) can be ignored during the interpretation of the BE-ESM data.[42] Therefore, sample electrical properties, such as surface conductance, are primarily investigated in this work. To identify the correlation between the ionic and electronic diffusion at the sample surface, complementary conductive AFM measurements are conducted on the LiNi$_{1/3}$Co$_{1/3}$Mn$_{1/3}$O$_2$ thin film cathode at different cycling stages. As an example, Figure 5a,b shows surface topography and the corresponding conductance image (at a sample voltage of +3 V) of the as-deposited LiNi$_{1/3}$Co$_{1/3}$Mn$_{1/3}$O$_2$ thin film cathode. In the surface conductance image, the brighter region represents higher current and hence the higher electronic conductance, while the darker region represents lower electronic conductance and thus higher resistance. As a result, the as-deposited thin film cathode exhibits excellent electronic conductance in most grain areas and only a few insulating regions concentrated at grain boundaries and intergranular deep cavities. The low surface conductance related to grain boundary features can also be identified in cycled thin film samples, indicating low electronic conductivity. Without considering the tip–sample contact resistance, the lower sample electronic conductance at grain boundaries can result in larger

effective potential drop, and thus higher field-driven force for ionic migration. Therefore, combining this result with the BE-ESM amplitude mappings (Figures 2 and 3), we find that the enhanced electrochemical strain concentrated at the grain boundaries is attributed to not only high ionic diffusion coefficient (concentration-driven) but also low electronic diffusion coefficient (field-driven). The results suggest that the decrease in electronic diffusion coefficient at grain boundaries can lead to preferred field-driven Li-ion migration as well as Li-ion accumulation, resulting in high ESM amplitude. Figure 5c shows the evolution of average surface conductance as a function of cycling number. The current values are obtained by averaging all values across a scanned area of 500×500 nm^2. It is clear that the surface electronic conductance has decreased with the increase of the cycling number. This reduction of the surface conductance is closely related to the observed capacity fading as well as the degradation of electrochemical activity. It is known that the electrode material in a Li-ion battery (*e.g.*, LiNi$_{1/3}$Co$_{1/3}$Mn$_{1/3}$O$_2$ thin film cathode) is a mixed electronic/ionic conductor. Therefore, the capacity fading is attributed to the degradation of both electronic diffusion and ionic diffusion capability. In this study, we have observed that the degradation in electrochemical strain is related to the ionic diffusion, while the surface conductance loss is closely related to the electronic diffusion during the charge/discharge cycling process; however, it is still difficult to make a clear distinction between these two contributions to the capacity fading, and this requires further studies in the future.

It is worth mentioning here that the ESM nanoscale mapping can also be applied to anode materials, which usually show different electrochemical characteristics from that of the cathode materials. In this work, however, the anode is room temperature deposited TiO$_2$, which has very fine structures. Since the Li-ion conductivity in liquid electrolyte (such as LiPF$_5$ in EC/DEC) is much larger than that of solid electrolyte (LiPON), it is not possible to fabricate the all-solid-state battery with the cathode as the top layer due to the different deposition temperature requirements for different layers.

Therefore, compared to that of the as-deposited cathode film, the ESM mapping on the TiO$_2$ thin film anode shows very small variations in strains between the different regions in the anode, hence, the results on the TiO$_2$ anode film are not presented in this paper. Nevertheless, the ESM measurement can be easily applied to other anode materials in all-solid-state batteries and can detect the variation of the strains if the anode materials can also show large ESM responses.

SUMMARY

To summarize, in this work, we used two advanced SPM techniques (*i.e.*, BE-ESM and c-AFM) to conduct the nanoscale mappings of the electrochemical activity on the LiNi$_{1/3}$Co$_{1/3}$Mn$_{1/3}$O$_2$ thin film cathode within an all-solid-state thin film Li-ion battery. The variations of electrochemical strain induced by ionic diffusion have been observed evidently on cathode surfaces, indicating inhomogeneous distribution of Li-ion diffusion and intercalation paths. For the thin film cathode, most of the high Li-ion concentration areas are localized at grain-boundary-like features and surface defects, respectively. Additionally, in order to investigate the galvanostatic cycling effect on the variations of ionic/electronic diffusion and electrochemical activity at the nanoscale, BE-ESM and c-AFM current mapping are conducted on the LiNi$_{1/3}$Co$_{1/3}$Mn$_{1/3}$O$_2$ thin film cathode at different cycling stages. The strong coupling between ionic/electronic diffusion coefficients, surface mechanical properties (elastic and damping behavior), as well as capacity fading of the LiNi$_{1/3}$Co$_{1/3}$Mn$_{1/3}$O$_2$ thin film cathode has also been established. This study allows visualizing electrochemical phenomena and Li-ion redistribution at various topographical features (grains/boundaries/cavities). In addition, we have established the direct relationships between the ionic/electronic diffusion and the microstructure of electrode materials, which can improve the understanding of electrochemical mechanisms underpinning the Li-ion battery operation and improve the battery performance.

EXPERIMENTAL SECTION

Materials. An all-solid-state thin film Li-ion battery was fabricated by magnetron sputtering on pure Ti (99.9%) substrate, which was highly polished to a mirror-like surface. In preparation of the thin film cathode, commercial LiNi$_{1/3}$Co$_{1/3}$Mn$_{1/3}$O$_2$ powders were first cold pressed into a pellet followed by sintering at 900 °C for 15 h to fabricate the target (2 in. diameter and 3 mm thick). The thin film cathode with a thickness of ~0.25 μm was deposited onto the substrate using radio frequency (RF) sputtering at 100 W in Ar/O$_2$ (3:1) atmosphere. The substrate temperature was kept at 700 °C. Afterward, the ~1 μm thick LiPON electrolyte was deposited by RF sputtering (60 W) in N$_2$ atmosphere at room temperature, using a commercial Li$_3$PO$_4$ target (Super Conductor Materials, Inc., 2 in. diameter and 3 mm thick). Finally, TiO$_2$ film (with a thickness of

the ~0.25 μm) was deposited from a titanium metal target (99.99% pure) as anode, also at room temperature.

Electrochemical Measurements. To verify the electrochemical functionality of the all-solid-state thin film Li-ion battery, a Au layer was deposited on top of the TiO$_2$ anode as current collector. Galvanostatic charge/discharge cycling test was carried out in the voltage range between 0 and 3.5 V with a discharge current density of 10 μAcm^{-2} and a charge current density of 5 μAcm^{-2}, using a battery test system (model MC-4, MACCOR, USA) in a four-probe vacuum chamber (MMR Technologies. Inc., CA). The electrochemical performance of the LiNi$_{1/3}$Co$_{1/3}$Mn$_{1/3}$O$_2$ thin film cathode was investigated by a half-cell test at ambient condition. The Swagelok-type cell, which consists of a LiNi$_{1/3}$Co$_{1/3}$Mn$_{1/3}$O$_2$ working electrode (1.0 cm^2 diameter), lithium foil counter electrode, and fluid electrolyte (1 M LiPF$_5$ in 1:1 ethylene carbonate

(EC) and diethyl carbonate (DEC) solution), was assembled in an Ar-filled glovebox (MBEAUN Glove Box Technology, Germany). The battery cells were then subjected to various galvanostatic charge/discharge cycles (10, 50, and 100 cycles) in the voltage range from 3.0 to 4.3 V and a constant current density of 10 μAcm^{-2}. The cycled cathode film was then dissembled and rinsed for SPM measurements.

SPM Measurements. BE-ESM measurements were conducted on a commercial SPM instrument (MPF-3D, Asylum Research, USA) equipped with a commercial band excitation (BE) control and data acquisition software (Asylum Research/Oak Ridge National Laboratory, USA). During the BE-ESM measurement, the conductive substrate was grounded, and the bias was applied through a Pt-coated Si tip (Electri-Lever, Olympus, Japan) in direct contact with the cathode surface without any coating. The cantilever has the resonance frequency about 75 kHz, a spring constant of 2 N m^{-1}, and a tip radius of ~15 nm. All measurements were conducted at room temperature in ambient atmosphere. Electrochemical strain mapping was performed with 6 V$_{AC}$ band excitation signal and a bandwidth of ~20 kHz centered at ~290 kHz. The BE-ESM parameters are extracted at each point of 128 × 128 point-grid in the 500 × 500 nm^2 area by fitting the response curves using an idealized mass-spring model, that is, the simple harmonic oscillator (SHO) method.[15] In the SHO approximation, the resonance frequencies, response amplitude, and Q-factor are fitted from the measured amplitude and phase curves and stored as images.

To test and image the electronic conductivity of the sample surface, conductive AFM measurement was performed using the same SPM instrument with a commercial conductive AFM module (ORCA, Asylum Research, USA). All of the c-AFM measurements were performed using a PtSi conductive tip (Nanosensors, Switzerland) with controlled sample voltage (~3 V). A surface topography image and a conductance image can be obtained simultaneously, while the tip scans over the sample surface; the conductance image represents the tip−sample current variations at a given sample voltage. At least three different areas in each sample are imaged by BE-ESM and c-AFM measurements.

Nanoindentation Measurements. The Young's modulus (E^*) of the LiNi$_{1/3}$Co$_{1/3}$Mn$_{1/3}$O$_2$ thin film cathode was determined using a commercial nanoindenter (Nano-Indenter XP, MTS Corporation, USA) with the continuous stiffness measurement option. All measurements were conducted under the strain-rate control (0.05 s^{-1}) using a standard Berkovich indenter (inclusion angle = 131°; estimated tip radius = 50 nm). At least 20 indents were made on each sample to get average values of Young's modulus.

Conflict of Interest: The authors declare no competing financial interest.

REFERENCES AND NOTES

1. Goodenough, J. B.; Kim, Y. Challenges for Rechargeable Li Batteries. *Chem. Mater.* **2010**, *22*, 587–603.
2. Liu, C.; Li, F.; Ma, L. P.; Cheng, H. M. Advanced Materials for Energy Storage. *Adv. Mater.* **2010**, *22*, E28–E62.
3. Ritchie, A. G. Recent Developments and Likely Advances in Lithium Rechargeable Batteries. *J. Power Sources* **2004**, *136*, 285–289.
4. Kalinin, S. V.; Balke, N. Local Electrochemical Functionality in Energy Storage Materials and Devices by Scanning Probe Miroscopies: Status and Perspectives. *Adv. Mater.* **2010**, *22*, E193–E209.
5. Nagpure, S. C.; Bhushan, B. Atomic Force Microscopy Studies of Aging Mechanisms in Lithium-Ion Batteries. In *Applied Scanning Probe Methods XIII: Biomimetics and Industrial Applications*; Bhushan, B., Fuchs, H., Eds.; Springer: Berlin, 2009; pp 203−233.
6. Balke, N.; Jesse, S.; Morozovska, A. N.; Eliseev, E.; Chung, D. W.; Kim, Y.; Adamczyk, L.; Garcia, R. E.; Dudney, N. J.; Kalinin, S. V. Nanoscale Mapping of Ion Diffusion in a Lithium-Ion Battery Cathode. *Nat. Nanotechnol.* **2010**, *5*, 749–754.
7. Balke, N.; Jesse, S.; Kim, Y.; Adamczyk, L.; Ivanov, I. N.; Dudney, N. J.; Kalinin, S. V. Decoupling Electrochemical Reaction and Diffusion Processes in Ionically-Conductive Solids on the Nanometer Scale. *ACS Nano* **2010**, *4*, 7349–7357.
8. Guo, S.; Jesse, S.; Kalnaus, S.; Balke, N.; Daniel, C.; Kalinin, S. V. Direct Mapping of Ion Diffusion Times on LiCoO$_2$ Surfaces with Nanometer Resolution. *J. Electrochem. Soc.* **2011**, *158*, A982–A990.
9. Jesse, S.; Balke, N.; Eliseev, E.; Tselev, A.; Dudney, N. J.; Morozovska, A. N.; Kalinin, S. V. Direct Mapping of Ionic Transport in a Si Anode on the Nanoscale: Time Domain Electrochemical Strain Spectroscopy Study. *ACS Nano* **2011**, *5*, 9682–9695.
10. Kalinin, S.; Balke, N.; Jesse, S.; Tselev, A.; Kumar, A.; Arruda, T. M.; Guo, S.; Proksch, R. Li-Ion Dynamics and Reactivity on the Nanoscale. *Mater. Today* **2011**, *14*, 548–558.
11. Morozovska, A. N.; Eliseev, E. A.; Balke, N.; Kalinin, S. V. Local Probing of Ionic Diffusion by Electrochemical Strain Microscopy: Spatial Resolution and Signal Formation Mechanisms. *J. Appl. Phys.* **2010**, *108*, 053712.
12. Morozovska, A. N.; Eliseev, E. A.; Kalinin, S. V. Electromechanical Probing of Ionic Currents in Energy Storage Materials. *Appl. Phys. Lett.* **2010**, *96*, 222906.
13. Chung, D. W.; Balke, N.; Kalinin, S. V.; Garcia, R. E. Virtual Electrochemical Strain Microscopy of Polycrystalline LiCoO$_2$ Films. *J. Electrochem. Soc.* **2011**, *158*, A1083–A1089.
14. Balke, N.; Jesse, S.; Kim, Y.; Adamczyk, L.; Tselev, A.; Ivanov, I. N.; Dudney, N. J.; Kalinin, S. V. Real Space Mapping of Li-Ion Transport in Amorphous Si Anodes with Nanometer Resolution. *Nano Lett.* **2010**, *10*, 3420–3425.
15. Jesse, S.; Kalinin, S. V. Band Excitation in Scanning Probe Microscopy: Sines of Change. *J. Phys. D: Appl. Phys.* **2011**, *44*, 1–16.
16. Jesse, S.; Kumar, A.; Kalinin, S. V.; Gannepali, A.; Proksch, R. Band Excitation Scanning Probe Microscopies. *Microsc. Today* **2010**, *18*, 34–40.
17. Kalinin, S.; Kumar, A.; Balke, N.; McCorkle, M.; Guo, S. L.; Arruda, T.; Jesse, S. ESM of Ionic and Electrochemical Phenomena on the Nanoscale. *Adv. Mater. Process.* **2011**, *169*, 30–34.
18. Soergel, E. Piezoresponse Force Microscopy (PFM). *J. Phys. D: Appl. Phys.* **2011**, *44*, 1–17.
19. Jesse, S.; Mirman, B.; Kalinin, S. V. Resonance Enhancement in Piezoresponse Force Microscopy: Mapping Electromechanical Activity, Contact Stiffness, and Q Factor. *Appl. Phys. Lett.* **2006**, *89*, 022906.
20. García, R.; Pérez, R. Dynamic Atomic Force Microscopy Methods. *Surf. Sci. Rep.* **2002**, *47*, 197–301.
21. Jesse, S.; Kalinin, S. V.; Proksch, R.; Baddorf, A. P.; Rodriguez, B. J. The Band Excitation Method in Scanning Probe Microscopy for Rapid Mapping of Energy Dissipation on the Nanoscale. *Nanotechnology* **2007**, *18*, 435503.
22. Ding, J. J.; Sun, Q. A.; Fu, Z. W. Layered Li(Ni$_{1/4}$Mn$_{1/2}$Co$_{1/3}$)O$_2$ as Cathode Material for All-Solid-State Thin-Film Rechargeable Lithium-Ion Batteries. *Electrochem. Solid State Lett.* **2010**, *13*, A105–A108.
23. Lu, C.-H.; Shen, B.-J. Electrochemical Characteristics of LiNi$_{1/3}$Co$_{1/3}$Mn$_{1/3}$O$_2$ Powders Prepared from Microwave-Hydrothermally Derived Precursors. *J. Alloys Compd.* **2010**, *497*, 159–165.
24. Shaju, K. M.; Bruce, P. G. Macroporous Li(Ni$_{1/3}$Co$_{1/3}$Mn$_{1/3}$)O$_2$: A High-Power and High-Energy Cathode for Rechargeable Lithium Batteries. *Adv. Mater.* **2006**, *18*, 2330–2334.
25. Choi, J.; Manthiram, A. Investigation of the Irreversible Capacity Loss in the Layered LiNi$_{1/3}$Mn$_{1/3}$Co$_{1/3}$O$_2$ Cathodes. *Electrochem. Solid State Lett.* **2005**, *8*, C102–C105.
26. Yabuuchi, N.; Ohzuku, T. Novel Lithium insertion Material of LiCo$_{1/3}$Ni$_{1/3}$Mn$_{1/3}$O$_2$ for Advanced Lithium-Ion Batteries. *J. Power Sources* **2003**, *119*, 171–174.
27. Yabuuchi, N.; Ohzuku, T. Electrochemical Behaviors of LiCo$_{1/3}$Ni$_{1/3}$Mn$_{1/3}$O$_2$ in Lithium Batteries at Elevated Temperatures. *J. Power Sources* **2005**, *146*, 636–639.

28. Kim, J.-M.; Chung, H.-T. The First Cycle Characteristics of Li[Ni$_{1/3}$Co$_{1/3}$Mn$_{1/3}$]O$_2$ Charged up to 4.7 V. *Electrochim. Acta* **2004**, *49*, 937–944.

29. Deng, C.; Zhang, S.; Fu, B. L.; Yang, S. Y.; Ma, L. Synthetic Optimization of Nanostructured Li[Ni$_{1/3}$Mn$_{1/3}$Co$_{1/3}$]O$_2$ Cathode Material Prepared by Hydroxide Coprecipitation at 273 K. *J. Alloys Compd.* **2010**, *496*, 521–527.

30. Yabuuchi, N.; Makimura, Y.; Ohzuku, T. Solid-State Chemistry and Electrochemistry of LiCo$_{1/3}$Ni$_{1/3}$Mn$_{1/3}$O$_2$ for Advanced Lithium-Ion Batteries III. Rechargeable Capacity and Cycleability. *J. Electrochem. Soc.* **2007**, *154*, A314–A321.

31. Li, D.; Kato, Y.; Kobayakawa, K.; Noguchi, H.; Sato, Y. Preparation and Electrochemical Characteristics of LiNi$_{1/3}$Mn$_{1/3}$Co$_{1/3}$O$_2$ Coated with Metal Oxides Coating. *J. Power Sources* **2006**, *160*, 1342–1348.

32. Yue, W. Z. Investigation of LiNi$_{1/3}$Co$_{1/3}$Mn$_{1/3}$O$_2$ Cathode Particles after 300 Discharge/Charge Cycling in a Lithium-Ion Battery by Analytical TEM. *J. Power Sources* **2008**, *183*, 316–324.

33. Oh, S. W.; Park, S.-H.; Sun, Y.-K. Hydrothermal Synthesis of Nano-Sized Anatase TiO$_2$ Powders for Lithium Secondary Anode Materials. *J. Power Sources* **2006**, *161*, 1314–1318.

34. Subramanian, V.; Karki, A.; Gnanasekar, K. I.; Eddy, F. P.; Rambabu, B. Nanocrystalline TiO$_2$ (Anatase) for Li-Ion Batteries. *J. Power Sources* **2006**, *159*, 186–192.

35. Wang, Y.; Wu, M.; Zhang, W. F. Preparation and Electrochemical Characterization of TiO$_2$ Nanowires as an Electrode Material for Lithium-Ion Batteries. *Electrochim. Acta* **2008**, *53*, 7863–7868.

36. Wu, M.-S.; Wang, M.-J.; Jow, J.-J.; Yang, W.-D.; Hsieh, C.-Y.; Tsai, H.-M. Electrochemical Fabrication of Anatase TiO$_2$ Nanostructure as an Anode Material for Aqueous Lithium-Ion Batteries. *J. Power Sources* **2008**, *185*, 1420–1424.

37. Natarajan, C.; Fukunaga, N.; Nogami, G. Titanium Dioxide Thin Film Deposited by Spray Pyrolysis of Aqueous Solution. *Thin Solid Films* **1998**, *322*, 6–8.

38. Tsai, Y. W.; Hwang, B. J.; Ceder, G.; Sheu, H. S.; Liu, D. G.; Lee, J. F. *In-Situ* X-ray Absorption Spectroscopic Study on Variation of Electronic Transitions and Local Structure of LiNi$_{1/3}$Co$_{1/3}$Mn$_{1/3}$O$_2$ Cathode Material during Electrochemical Cycling. *Chem. Mater.* **2005**, *17*, 3191–3199.

39. Chen, Q. N.; Liu, Y. Y.; Liu, Y. M.; Xie, S. H.; Cao, G. Z.; Li, J. Y. Delineating Local Electromigration for Nanoscale Probing of Lithium Ion Intercalation and Extraction by Electrochemical Strain Microscopy. *Appl. Phys. Lett.* **2012**, *101*, 063901.

40. Killgore, J. P.; Yablon, D. G.; Tsou, A. H.; Gannepalli, A.; Yuya, P. A.; Turner, J. A.; Proksch, R.; Hurley, D. C. Viscoelastic Property Mapping with Contact Resonance Force Microscopy. *Langmuir* **2011**, *27*, 13983–13987.

41. Stan, G.; Krylyuk, S.; Davydov, A. V.; Vaudin, M. D.; Bendersky, L. A.; Cook, R. F. Contact-Resonance Atomic Force Microscopy for Nanoscale Elastic Property Measurements: Spectroscopy and Imaging. *Ultramicroscopy* **2009**, *109*, 929–936.

42. Balke, N.; Kalnaus, S.; Dudney, N. J.; Daniel, C.; Jesse, S.; Kalinin, S. V. Local Detection of Activation Energy for Ionic Transport in Lithium Cobalt Oxide. *Nano Lett.* **2012**, *12*, 3399–3403.